iScience

CellPress
OPEN ACCESS

Article

The winged helix domain of MORF binds CpG islands and the TAZ2 domain of p300

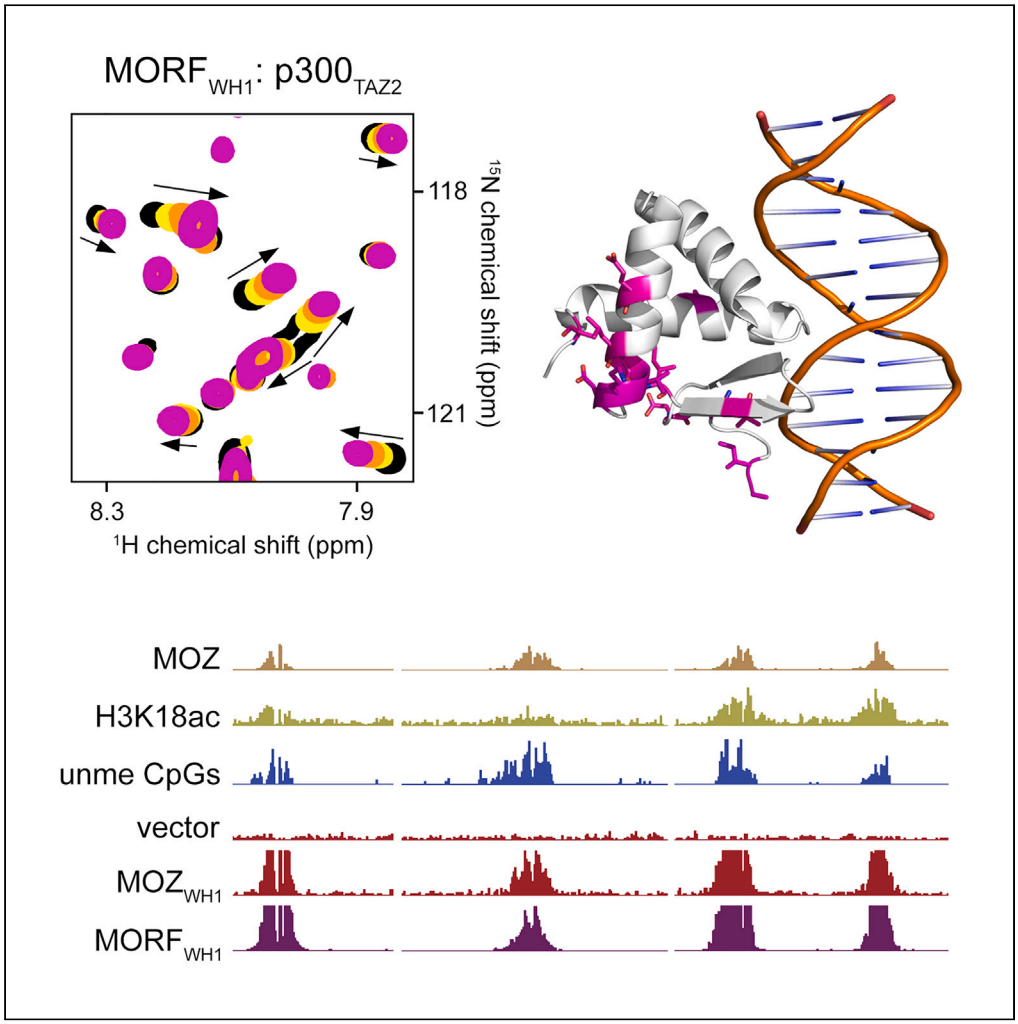

Dustin C. Becht, Akinori Kanai, Soumi Biswas, ..., Xiaobing Shi, Akihiko Yokoyama, Tatiana G. Kutateladze

tatiana.kutateladze@cuanschutz.edu

Highlights

The winged helix domain of MORF (MORF$_{WH1}$) binds the TAZ2 domain of p300

MORF$_{WH1}$ occupies the transactivation domain-binding site of TAZ2

MORF$_{WH1}$ independently engages TAZ2 and CpG DNA

MORF$_{WH1}$ localizes to H3K18ac- and CpG-rich promoters of target genes

Becht et al., iScience *27*, 109367
April 19, 2024
https://doi.org/10.1016/j.isci.2024.109367

iScience

CellPress
OPEN ACCESS

Article

The winged helix domain of MORF binds CpG islands and the TAZ2 domain of p300

Dustin C. Becht,[1] Akinori Kanai,[2] Soumi Biswas,[1] Mohamed Halawa,[1] Lei Zeng,[3,4] Khan L. Cox,[5] Michael G. Poirier,[5] Ming-Ming Zhou,[6] Xiaobing Shi,[7] Akihiko Yokoyama,[8] and Tatiana G. Kutateladze[1,9,*]

SUMMARY

Acetylation of histones by lysine acetyltransferases (KATs) provides a fundamental mechanism by which chromatin structure and transcriptional programs are regulated. Here, we describe a dual binding activity of the first winged helix domain of human MORF KAT ($MORF_{WH1}$) that recognizes the TAZ2 domain of p300 KAT ($p300_{TAZ2}$) and CpG rich DNA sequences. Structural and biochemical studies identified distinct DNA and $p300_{TAZ2}$ binding sites, allowing $MORF_{WH1}$ to independently engage either ligand. Genomic data show that $MORF/MOZ_{WH1}$ colocalizes with H3K18ac, a product of enzymatic activity of p300, on CpG rich promoters of target genes. Our findings suggest a functional cooperation of MORF and p300 KATs in transcriptional regulation.

INTRODUCTION

Histone lysine acetylation is a major posttranslational modification that regulates chromatin structure and dynamics and is associated with a more accessible genome and active transcription.[1,2] In mammals, acetylation is catalyzed by three families of lysine acetyltransferases (KATs) or traditionally referred to as histone acetyltransferases (HATs): the GNAT, p300/CBP, and MYST families. The MYST family of KATs contains five members, including MOZ (monocytic leukemic zinc-finger protein; or KAT6A) and MORF (MOZ-related factor; or KAT6B).[3] MOZ and MORF KATs are essential in embryogenesis and hematopoiesis and implicated in chromosomal translocations which are linked to aggressive forms of leukemia.[4–6] Aberrant functions of MOZ/MORF have also been associated with developmental and neurological disorders and intellectual disability.[7–9]

MORF is a catalytic subunit of the four-core component complex that bears the same name, the MORF complex, and acetylates primarily lysine 23 of histone H3 (H3K23ac).[10] The other three subunits of the complex include BRPF1 (bromodomain PHD finger protein 1), ING4/5 (inhibitor of growth 4/5), and MEAF6 (MYST/Esa1-associated factor 6). Much like the MORF complex, the MOZ complex contains BRPF1, ING4/5, and MEAF6 but the fourth subunit is MOZ. MORF and MOZ KATs have similar domain architecture, consisting of two winged helix domains (WH1 and WH2), a double PHD finger (DPF) which interacts with acylated lysine 14 of histone H3 (H3K14acyl) and DNA, and the catalytic MYST domain[11–16] (Figure 1A). Both WH1 and WH2 of MOZ/MORF bind DNA, and WH1 exhibits a high degree of specificity for unmethylated CpG.[17,18] Genetic and biochemical studies show that the DNA binding function of WHs is required for the recruitment of MORF to target genes and H3K23 acetylation.[18]

p300 and its paralog CREB-binding protein (CBP), also known as KAT3B and KAT3A, respectively, are transcriptional coactivators.[19–21] p300/CBP promote gene expression through acetylating histone H3K18 and H3K27 but can also acetylate non-histone proteins.[22,23] Additionally, p300/CBP act as scaffolding proteins for the assembly of large transcription complexes and connect these complexes to the RNA polymerase II transcription machinery.[24,25] Because p300/CBP are commonly found at regulatory DNA elements, particularly enhancers, their genomic localization or elevated levels of H3K18ac and H3K27ac serve as predictive markers of active enhancers.[26,27] Given the function of CBP/p300 as transcriptional regulators, these HATs play vital roles in cell proliferation, differentiation, apoptosis, and development.[24] In mouse models, knockout of either p300 or CBP leads to embryonic lethality, and mutations in these KATs are associated with various cancers.[28–31]

The catalytic core of p300/CBP consists of a bromodomain (BD), the RING and PHD fingers, the HAT domain, and the adjacent ZZ and TAZ2 zinc fingers.[23,32] Each of these domains directly or indirectly affects enzymatic activity and substrate selectivity through intra- and

[1]Department of Pharmacology, University of Colorado School of Medicine, Aurora, CO 80045, USA
[2]Department of Computational Biology and Medical Sciences, Graduate School of Frontier Sciences, the University of Tokyo, Kashiwa, Chiba 277-0882, Japan
[3]Bethune Institute of Epigenetic Medicine, First Hospital of Jilin University, Changchun 130061, China
[4]International Center of Future Science, Jilin University, Changchun 130012, China
[5]Department of Physics, Ohio State University, Columbus, OH 43210, USA
[6]Department of Pharmacological Sciences, Icahn School of Medicine at Mount Sinai, New York, NY 10029, USA
[7]Department of Epigenetics, Van Andel Institute, Grand Rapids, MI 49503, USA
[8]Tsuruoka Metabolomics Laboratory, National Cancer Center, Tsuruoka, Yamagata 997-0052, Japan
[9]Lead contact
*Correspondence: tatiana.kutateladze@cuanschutz.edu
https://doi.org/10.1016/j.isci.2024.109367

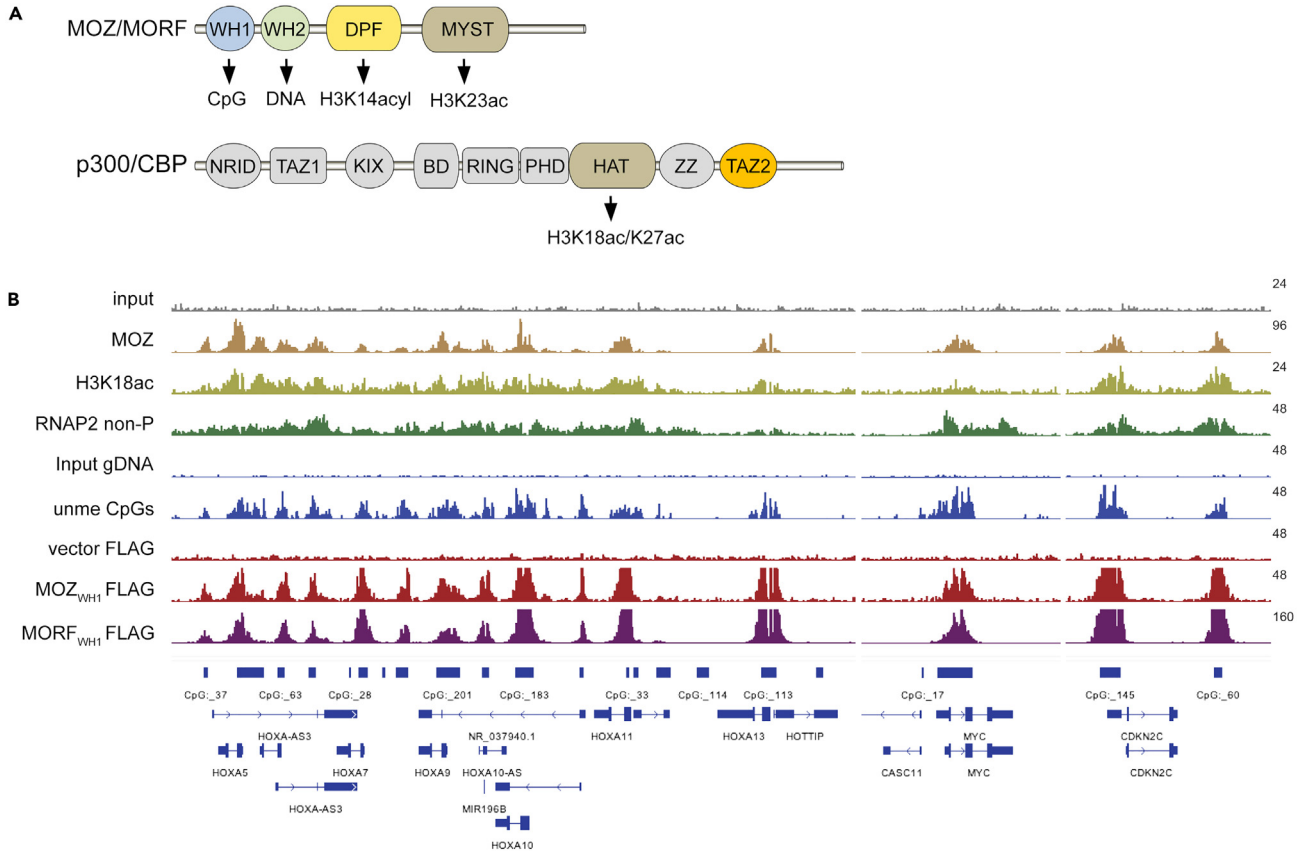

Figure 1. MOZ_{WH1} and $MORF_{WH1}$ colocalize with H3K18ac and unmethylated CpGs on promoters of target genes

(A) Domain architecture of MOZ/MORF and p300 KATs. Binding partners of the domains in MOZ/MORF and the products of enzymatic activities of MOZ/MORF and p300 KATs are labeled.

(B) Representative images of genomic localization of endogenous full-length MOZ and RNAP2 non-P, H3K18ac, unmethylated CpG and FLAG-tagged MOZ_{WH1} and $MORF_{WH1}$ at the indicated loci in HEK293T cells. ChIP signals were visualized using the Integrative Genomics Viewer (The Broad Institute).

intermolecular interactions. p300-mediated acetylation and the association of p300 with chromatin require binding of BD to acetylated histones.[33,34] The RING-PHD fingers region has an autoinhibitory function, whereas an autoregulatory loop within the HAT domain acts as a pseudo-substrate.[32,35,36] The ZZ domain of p300 binds to histone H3 tail, stimulating *in cis* acetylation of H3K27 and H3K18, and the TAZ2 domain interacts with transcription factors and contributes to autoregulation.[34,37–39]

Here, we report that the first winged helix of MORF ($MORF_{WH1}$) binds the TAZ2 domain of p300 ($p300_{TAZ2}$) and CpG containing DNA sequences *in vitro* and occupies H3K18ac- and CpG-rich promoters of target genes *in vivo*.

RESULTS AND DISCUSSION

$MORF_{WH1}$ and MOZ_{WH1} localize to H3K18ac-rich CpGs

We have previously shown that the acetyltransferase MORF catalyzes acetylation of lysine 23 in histone H3, producing the epigenetic mark H3K23ac, whereas its DPF domain ($MORF_{DPF}$) associates with H3K14acyl.[10,13] We also found that while H3K23ac and H3K14ac represent the third most abundant co-exist combination of acetylated marks on histone H3, the co-existence frequency of H3K14ac and H3K18ac is 4-fold higher and the co-existence frequency of H3K23ac and H3K18ac is 2-fold higher.[10] To elucidate the relationship with H3K18ac, we examined genomic localization of endogenous full-length MOZ and H3K18ac in human HEK293T cells using chromatin immunoprecipitation coupled with deep sequencing (ChIP-seq) assays. As shown in Figure 1B, full-length MOZ co-localized with H3K18ac and non-phosphorylated RNA polymerase II (RNAP2 non-P) at promoters of target genes, including *HOXA9*, *MYC*, and *CDKN2C*. Furthermore, the localization pattern of full-length MOZ mirrored the localization pattern of the isolated winged helix domains, FLAG-tagged MOZ_{WH1} and $MORF_{WH1}$, suggesting that this domain is essential in engaging with H3K18ac-rich regions of individual genes (Figure 1B).

Further analysis of ChIP-seq revealed that the binding sites of full-length MOZ and MOZ_{WH1} genome-wide cluster at the promoters harboring unmethylated CpGs, supporting previous findings.[17,18] The signals were centered around the transcription start sites (TSS) and correlated well with the distribution of H3K18ac and RNAP2 non-P (Figure 2A). The cumulative ChIP signals of H3K18ac within a 1 kb

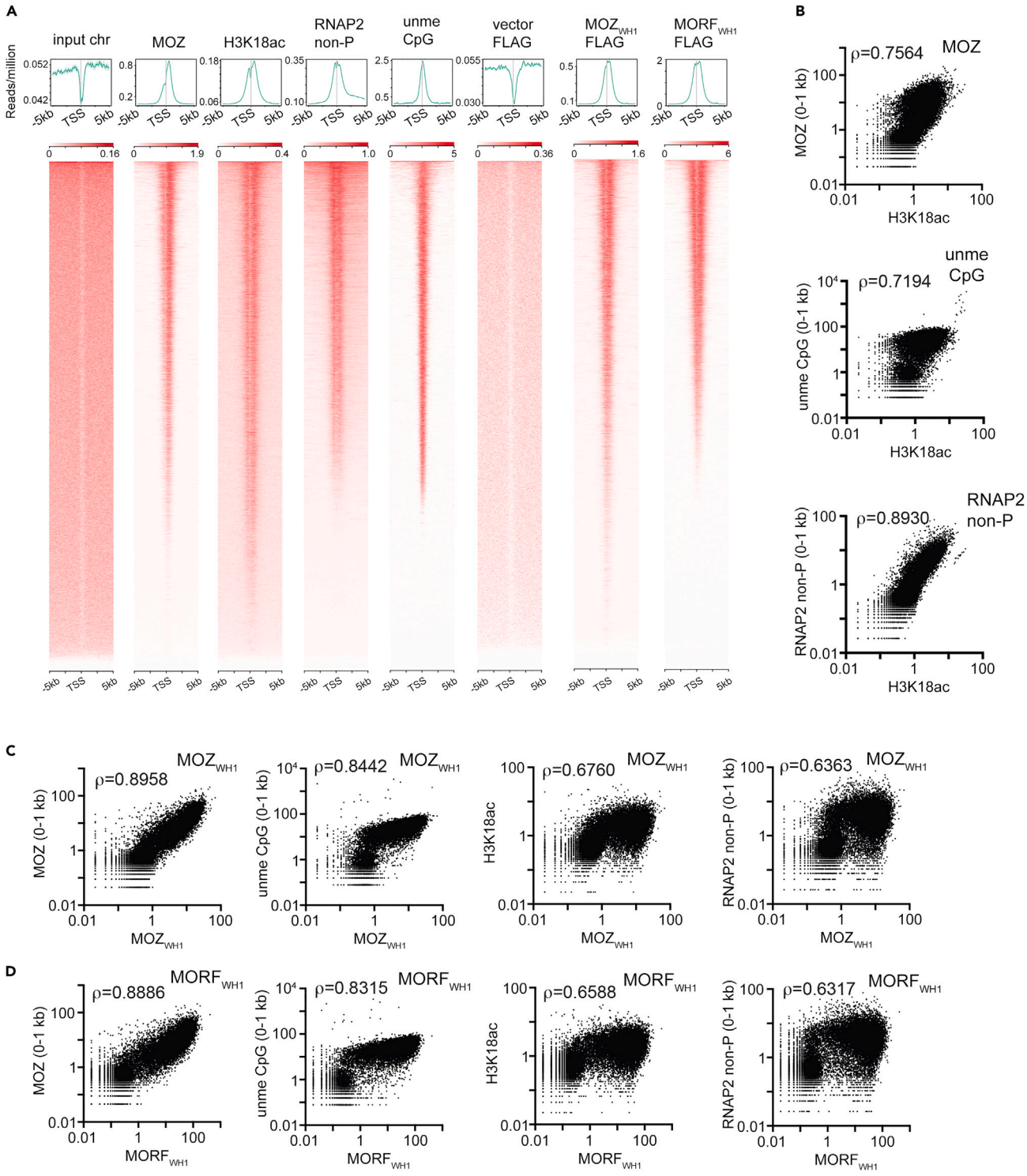

Figure 2. MOZ$_{WH1}$ and MORF$_{WH1}$ colocalize with H3K18ac and unmethylated CpGs genome wide

(A) Distribution patterns of ChIP signals near the transcriptional start sites (TSSs). ChIP signals within the 5 kb range of each TSS were plotted using the ngsplot software.

(B–D) Correlations of the ChIP signal intensities. ChIP-seq tags of the indicated proteins and H3K18ac were clustered into a 1-kb bin (0 to +1 kb from the TSS) and are presented as XY scatterplots. Spearman's rank correlation coefficient (ρ) is shown.

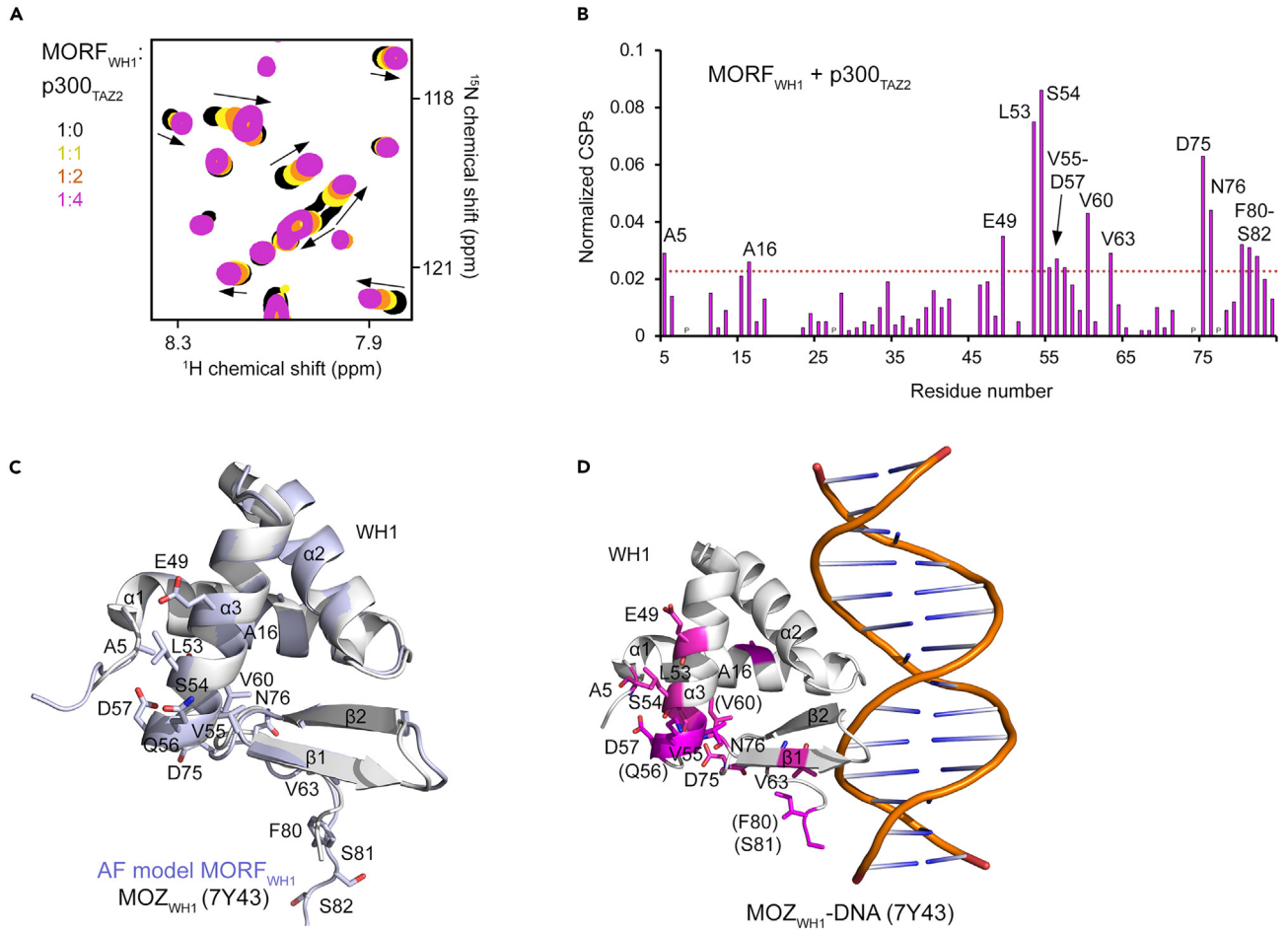

Figure 3. MORF$_{WH1}$ binds to p300$_{TAZ2}$

(A) Overlaid ^{1}H,^{15}N HSQC spectra of ^{15}N-labeled MORF$_{WH1}$ collected in the absence (black) and presence of increasing amounts of p300$_{TAZ2}$. Spectra are color coded according to the MORF$_{WH1}$:p300$_{TAZ2}$ molar ratio.

(B) Normalized CSPs observed in ^{1}H,^{15}N HSQC spectra of MORF$_{WH1}$ in the presence of four molar equivalents of p300$_{TAZ2}$ are shown as histogram per MORF$_{WH1}$ residue. The dotted line indicates the cutoff for residues to be considered perturbed. "p"- Pro.

(C) Superimposed AF model of MORF$_{WH1}$ from UniProt (Q8WYB5) (blue) and the crystal structure of the DNA-bound MOZ$_{WH1}$ (PDB: 7Y43) (gray). The most perturbed residues in (B) of MORF$_{WH1}$ are shown as sticks.

(D) CSPs in MORF$_{WH1}$ induced by p300$_{TAZ2}$ are mapped onto the structure of DNA-bound MOZ$_{WH1}$ (PDB: 7Y43), colored magenta and labeled. DNA is shown in a stick diagram.

downstream region of each TSS plotted against signals of MOZ, unmethylated CpGs, and RNAP2 non-P showed a high degree of correlation (Figure 2B). Notably, the signals of individual domains, MOZ$_{WH1}$ and MORF$_{WH1}$, also correlated with the signals of H3K18ac, unmethylated CpGs, and RNAP2 non-P, suggesting a WH1-dependent localization of MOZ/MORF at H3K18ac- and CpG-rich sites genome-wide (Figures 2C and 2D).

MORF$_{WH1}$ binds to p300$_{TAZ2}$

The strong genomic correlation of MOZ $_{WH1}$ and MORF$_{WH1}$ with H3K18ac, a product of the enzymatic activity of p300, prompted us to evaluate whether WH1 directly contacts p300. Analysis of amino acid sequences of MOZ$_{WH1}$ and MORF$_{WH1}$, which are overall almost identical, pointed to the presence of a hydrophobic motif encompassing first 17 residues of this domain in both MORF and MOZ (Figure S1). Similar hydrophobic sequences have been shown to be recognized by p300$_{TAZ2}$ and are named TADs (transactivation domains).[29] To assess whether MORF$_{WH1}$ is a TAD ligand of p300$_{TAZ2}$, we carried out NMR titration experiments. We generated ^{15}N-labeled MORF$_{WH1}$ and collected its ^{1}H,^{15}N HSQC (heteronuclear single quantum coherence) spectra while unlabeled p300$_{TAZ2}$ was titrated in. Addition of p300$_{TAZ2}$ resulted in chemical shift perturbations (CSPs) in the spectra of MORF$_{WH1}$, indicating formation of the complex between MORF$_{WH1}$ and p300$_{TAZ2}$ (Figure 3A).

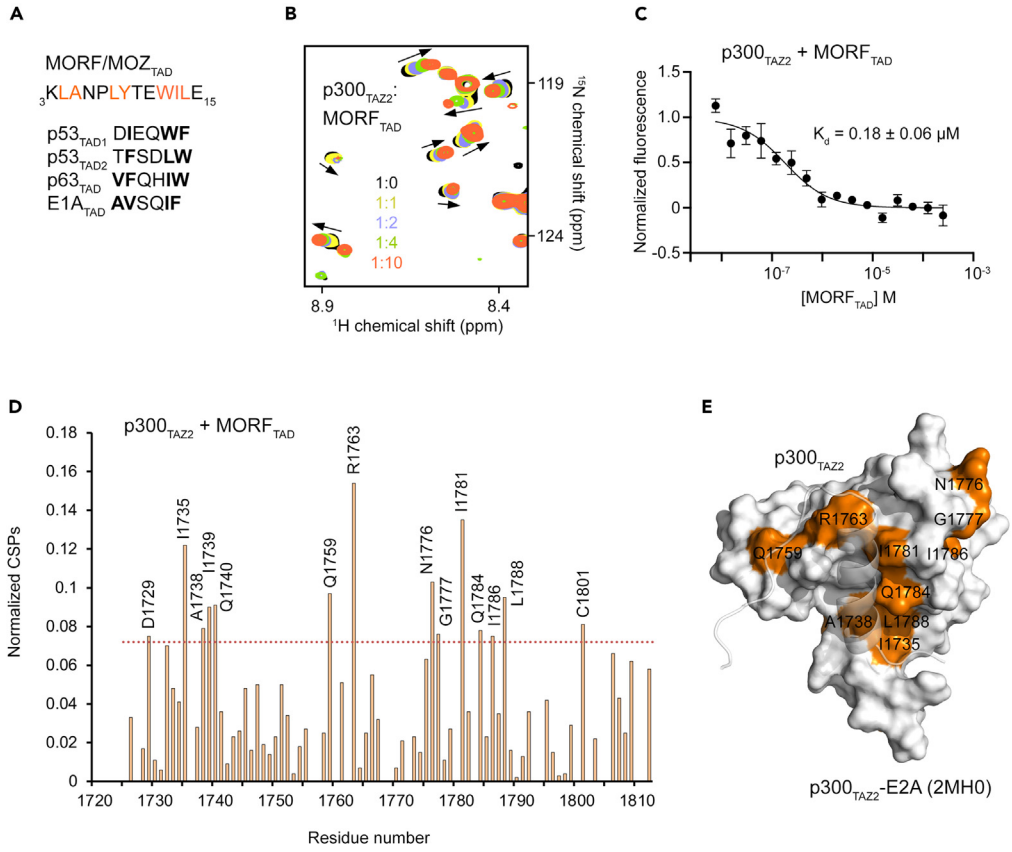

Figure 4. The TAD motif in MORF$_{WH1}$ is recognized by p300$_{TAZ2}$

(A) Sequences of the TAD motifs in the indicated proteins. Hydrophobic residues in the MORF/MOZ sequence are highlighted orange.

(B) Overlaid ^{1}H,^{15}N HSQC spectra of ^{15}N-labeled p300$_{TAZ2}$ collected in the absence (black) and presence of increasing amounts of the MORF$_{TAD}$ peptide. Spectra are color-coded according to the protein:peptide molar ratio.

(C) MST binding curve for the interaction of p300$_{TAZ2}$-His with the MORF$_{TAD}$ peptide. Data and the K_d value represent the average ± SEM of three independent experiments.

(D) Normalized CSPs observed in ^{1}H,^{15}N HSQC spectra of p300$_{TAZ2}$ in the presence of 10 molar equivalents of the MORF$_{TAD}$ peptide per p300$_{TAZ2}$ residue. The dotted line indicates the cutoff for residues to be considered perturbed.

(E) CSPs in p300$_{TAZ2}$ induced by MORF$_{TAD}$ are mapped onto the structure of p300$_{TAZ2}$ in complex with E2A (PDB: 2MH0), colored orange and labeled. E2A-AD1 in the binding pocket of p300$_{TAZ2}$ is depicted in a transparent ribbon diagram.

To identify the residues of MORF$_{WH1}$ involved in the contact with p300$_{TAZ2}$, we carried out triple resonance NMR experiments on uniformly ^{13}C,^{15}N-labeled MORF$_{WH1}$ and assigned backbone amide resonances of MORF$_{WH1}$. The assignment for the region from Q23 to K84 of MORF$_{WH1}$ was largely complete, but we were unable to unambiguously assign the hydrophobic amino-terminal region, particularly N6-T10 and K19-K22 of MORF$_{WH1}$ (Figure 3B). This region of MORF$_{WH1}$ likely folds into the first helix, α1, as suggested an overlay of the crystal structure of MOZ$_{WH1}$ (PDB 7Y43)[17] and the AlphaFold-derived model of MORF$_{WH1}$ (Figure 3C). To define the binding interface, we plotted CSPs observed in ^{1}H,^{15}N HSQC spectra of MORF$_{WH1}$ upon addition of p300$_{TAZ2}$ per residue (Figure 3B). We found that the tip of MORF$_{WH1}$, formed by the loop preceding α1 (A5), the end of α3 (L53, S54, V55, Q56, and D57), the loop connecting α3 and the β1 strand (V60), and the loop following the β2 strand (D75 and N76), was substantially perturbed and likely represents a binding interface with p300$_{TAZ2}$ (Figures 3B and 3C). Mapping the most perturbed residues onto the structure of MOZ$_{WH1}$ in complex with CpG-DNA (PDB 7Y43)[17] also suggested that the p300$_{TAZ2}$ binding site of MORF$_{WH1}$ and the DNA binding site of MORF$_{WH1}$ are on the opposite sides of this domain (Figure 3D).

MORF$_{TAD}$ occupies the TAD-binding site of p300$_{TAZ2}$

To gain insight into the binding mechanism, we investigated whether the α1 helix of MORF$_{WH1}$, which contains a potential TAD motif for p300$_{TAZ2}$ but lacks backbone amide assignments, is in direct contact with p300$_{TAZ2}$. Notably, over a dozen solution NMR structures of p300$_{TAZ2}$ in complex with TADs from various proteins have been determined, and all show that the ligand, the TAD, is an amphipathic α-helix that contains a hydrophobic motif, *hxxhh* or *hh/axxh/ah/a*, where *h* is a hydrophobic residue, *a* is an aromatic residue, and x is any residue (Figure 4A). A stepwise addition of the unlabeled MORF peptide (aa 3–23 of MORF) to ^{15}N-labeled p300$_{TAZ2}$ led to CSPs in ^{1}H,^{15}N HSQC

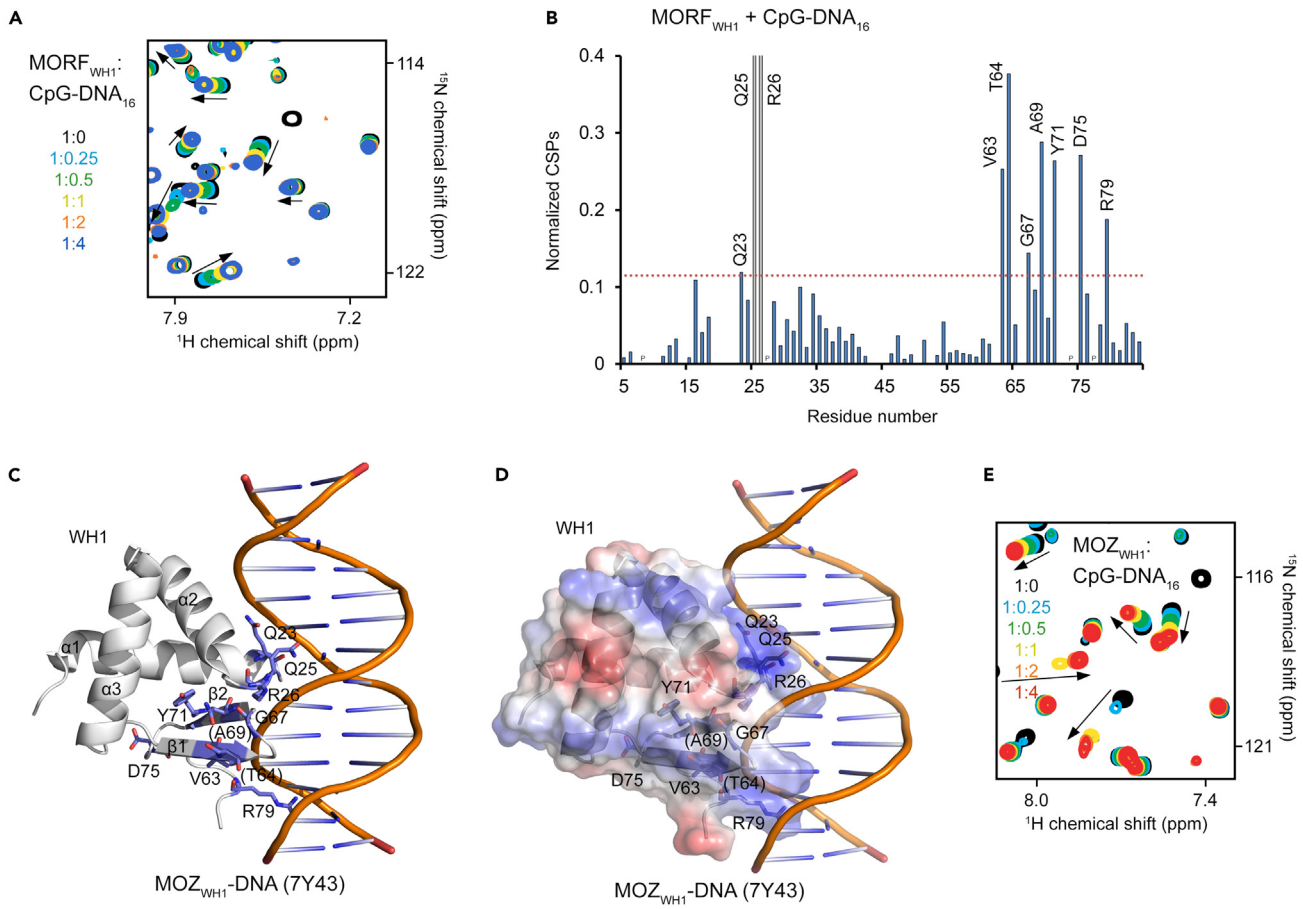

Figure 5. MORF$_{WH1}$ and MOZ $_{WH1}$ bind to CpG-rich DNA

(A) Overlayed ^{1}H,^{15}N HSQC spectra of ^{15}N-labeled MORF$_{WH1}$ collected in the absence (black) and presence of increasing amounts of CpG-DNA$_{16}$. Data are taken from Becht et al.[18] Spectra are color-coded according to the protein:DNA molar ratio.

(B) Normalized CSPs observed in ^{1}H,^{15}N HSQC spectra of MORF$_{WH1}$ the presence of four molar equivalents of CpG-DNA$_{16}$ per MORF$_{WH1}$ residue. The dotted line indicates the cutoff for residues to be considered perturbed. "p"- Pro.

(C and D) CSPs in MORF$_{WH1}$ induced by CpG-DNA$_{16}$ are mapped onto the structure of DNA-bound MOZ$_{WH1}$ (PDB: 7Y43, shown as a ribbon (C) and surface (D)), colored blue and labeled. Electrostatic surface potential of MOZ$_{WH1}$, with blue and red colors representing positive and negative charges, respectively, is shown in a transparent diagram in (D). DNA is shown in a stick diagram.

(E) Overlayed ^{1}H,^{15}N HSQC spectra of ^{15}N-labeled MOZ$_{WH1}$ collected in the absence (black) and presence of increasing amounts of CpG-DNA$_{16}$. Spectra are color-coded according to the protein:DNA molar ratio.

spectra of p300$_{TAZ2}$, indicative of the interaction with this peptide (from here on referred to as MORF$_{TAD}$) (Figure 4B). In agreement, microscale thermophoresis (MST) measurements for the interaction of p300$_{TAZ2}$ and MORF$_{TAD}$ yielded a K_d (dissociation constant) of 0.18 μM, which was in the range of binding affinities observed for the association of p300$_{TAZ2}$ with TADs from other proteins[29,39,40] (Figure 4C).

To delineate the binding interface, we assigned the apo-state of p300$_{TAZ2}$ and plotted CSPs induced in p300$_{TAZ2}$ by MORF$_{TAD}$ per residue (Figure 4D). The most perturbed p300$_{TAZ2}$ residues, such as D1729, I1735, A1738, I1739, and Q1740 of the α1 helix; Q1759 and R1763 of the α2 helix; N1776 and G1777 in an α-helical turn prior to α3; and I1781, Q1784, I1786, and L1788 of the α3 helix, were then mapped onto the surface of the solution structure of p300$_{TAZ2}$ bound to the E2A$_{TAD}$ peptide (PDB 2MH0).[41] As shown in Figure 4E, these most perturbed residues outlined the MORF$_{TAD}$ binding site, which corresponds to the canonical hydrophobic groove created by all three α helices of p300$_{TAZ2}$ and universally occupied by TADs.

Distinct p300$_{TAZ2}$ and DNA binding sites of MORF$_{WH1}$

A model shown in Figure 3D suggested that p300$_{TAZ2}$ binds to the side of MORF$_{WH1}$ which is opposite to the side where DNA is bound. To validate this model and confirm the mechanism by which MORF$_{WH1}$ associates with DNA, we analyzed CSPs in MORF$_{WH1}$ induced by a 16 bp CpG dsDNA (CpG-DNA$_{16}$) in previously reported ^{1}H,^{15}N HSQC assay[18] (Figures 5A and S2). In solution, CpG-DNA$_{16}$ caused CSPs primarily in two regions, encompassing residues Q23-R26 and V63-R79 of MORF$_{WH1}$ (Figure 5B). Mapping the most perturbed

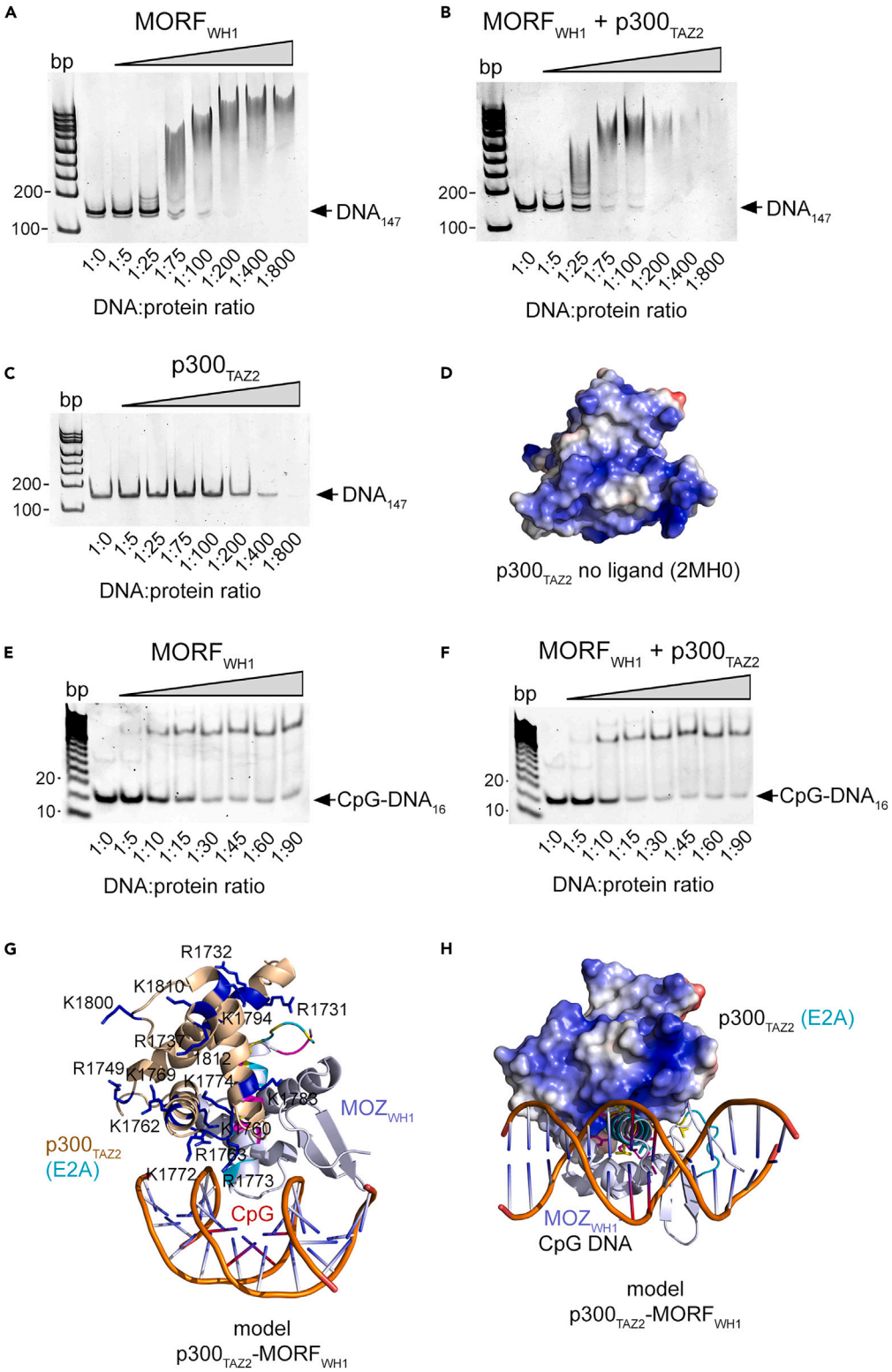

Figure 6. $MORF_{WH1}$ has independent binding sites for $p300_{TAZ2}$ and CpG DNA

(A and B) EMSAs of 601 DNA_{147} with increasing amounts of $MORF_{WH1}$ in the absence (A) and presence (B) of 2 μM $p300_{TAZ2}$. DNA:protein ratio is shown below the gel images.

(C) EMSAs of 601 DNA_{147} with increasing amounts of $p300_{TAZ2}$.

Figure 6. *Continued*

(D) Electrostatic surface potential of $p300_{TAZ2}$ without the ligand, with blue and red colors representing positive and negative charges, respectively (PDB: 2MH0).
(E and F) EMSAs of CpG-DNA_{16} with increasing amounts of $MORF_{WH1}$ in the absence (E) and presence (F) of 2 μM $p300_{TAZ2}$.
(G and H) A model for the interaction of MOZ/$MORF_{WH1}$ with CpG-rich DNA and $p300_{TAZ2}$. The α1 helix of MOZ_{WH1} (blue) in complex with DNA (PDB: 7Y43) is superimposed with E2A (cyan) from the structure of $p300_{TAZ2}$ (wheat) in complex with E2A peptide (PDB: 2MH0). Hydrophobic residues in MOZ/$MORF_{WH1}$ and E2A are shown as sticks and colored magenta and yellow, respectively. $p300_{TAZ2}$ is shown in a ribbon (G) and surface (H) diagrams. CpG sequence is red.

residues onto the structure of MOZ_{WH1} bound to DNA (PDB 7Y43)[17] showed that these residues are located in the loop connecting α1 and α2, the β hairpin, and the loop following the β2 strand (Figure 5C). The CpG DNA-binding interface of $MORF_{WH1}$ identified by NMR CSP analysis correlated well with the DNA-binding site observed in the crystal structure of MOZ_{WH1} (Figure 5D), and a lack of significant CSPs in $MORF_{WH1}$ upon titration with AT-rich DNA corroborated the high degree of specificity of this domain toward CpG DNA (Figure S2). Overlays of the NMR spectra of $MORF_{WH1}$ and MOZ_{WH1} upon titration with CpG-DNA_{16} showed that saturation was reached at the same protein:DNA ratio of 1:2, implying a similar strength of these interactions (Figures 5A–5E and S2), and comparable affinities of $MORF_{WH1}$ and MOZ_{WH1} toward nucleosomes and the preference for the nucleosome with a linker DNA[18] were confirmed by fluorescence polarization measurements (Figure S3).

$p300_{TAZ2}$ does not inhibit DNA binding by $MORF_{WH1}$

To determine if binding of $p300_{TAZ2}$ affects the DNA binding ability of $MORF_{WH1}$, we examined the association of $MORF_{WH1}$ with 147 bp 601 Widom DNA (DNA_{147}) in electrophoretic mobility shift assay (EMSA). Increasing amounts of $MORF_{WH1}$ in the presence and absence of 2 μM of $p300_{TAZ2}$ were incubated with DNA_{147}, and the reaction mixtures were resolved on a native polyacrylamide gel (Figures 6A and 6B). A gradual increase of $MORF_{WH1}$ concentration led to the shift of the DNA_{147} band, indicating that $MORF_{WH1}$ forms a complex with DNA (Figure 6A). The presence of $p300_{TAZ2}$ did not reduce binding of $MORF_{WH1}$ to DNA and had a slightly positive effect on the shifting pattern (Figure 6B). Interestingly, EMSA assays revealed that $p300_{TAZ2}$ itself is capable of binding to DNA, which may explain the slight increase in the DNA binding by $MORF_{WH1}$ when $p300_{TAZ2}$ is present (Figure 6C). Although DNA binding activity of $p300_{TAZ2}$ has not been yet characterized, a highly positively charged surface of this domain (pI of 9.9) suggests that $p300_{TAZ2}$ can make favorable electrostatic contacts with the negatively charged DNA. Similar results, i.e., a slight increase in DNA binding activity, were obtained for the association of $MORF_{WH1}$ with CpG-DNA_{16} (Figures 6E, 6F, and S4). Titration of unlabeled $p300_{TAZ2}$ into NMR sample of CpG-DNA_{16}-bound ^{15}N-labeled $MORF_{WH1}$ led to a decrease in intensity of the $MORF_{WH1}$ amide resonances, further substantiating the formation of the large three-component $MORF_{WH1}$-CpG-$p300_{TAZ2}$ complex (Figure S5). Collectively, these data suggest that $MORF_{WH1}$ can independently engage either ligand, $p300_{TAZ2}$ or DNA, or bind concomitantly both.

In conclusion, in this study we show that the first winged helix domain of human acetyltransferase MORF binds $p300_{TAZ2}$ and CpG DNA. NMR CSP analysis outlines non-overlapped $p300_{TAZ2}$- and DNA-binding sites of $MORF_{WH1}$, suggesting that $MORF_{WH1}$ can interact with either ligand or both. $MORF_{WH1}$ is a member of an atypical winged helix family that recognizes CpG DNA through a mechanism distinctly different from that of typical winged helix domains. While a typical winged helix domain binds to DNA primarily via its α3 helix,[42] $MORF_{WH1}$, similarly to MOZ_{WH1},[17] engages the CpG sequence through the α1-α2 loop, β-hairpin and the loop following β2. Interestingly, the hydrophobic α-helical $E2A_{TAD}$ from the structure of $p300_{TAZ2}$-E2A complex[41] overlays well with the hydrophobic α1 helix of MOZ_{WH1} from the structure of the MOZ_{WH1}-DNA complex[17] (Figures 6G and 6H). This model suggests that no steric hindrance would occur when $MORF_{WH1}$ forms the complex with both $p300_{TAZ2}$ and DNA. Furthermore, in this model, formation of the $MORF_{WH1}$-$p300_{TAZ2}$ complex would position the highly positively charged α2-α3 loop and the α2 helix of $p300_{TAZ2}$ in close proximity to DNA, which can strengthen the contacts of $MORF_{WH1}$ with DNA. $MORF_{WH1}$ is followed by three other closely located domains: a typical DNA-binding winged helix, $MORF_{WH2}$, $MORF_{DPF}$ that binds H3K14acyl and DNA, and the catalytic $MORF_{MYST}$ domain that acetylates H3K23.[10,13,18] How these multiple contacts with DNA, histones, p300, and other subunits of the MORF complex mediate biological functions of the complex in normal and pathogenic cell processes require further investigation. Elucidating the molecular basis of the MORF-p300-chromatin interactions is also essential to better understand the etiology of leukemias and hematological diseases associated with aberrant acetylation levels and may pave the way for the development of novel therapies to prevent or treat these diseases.

Limitations of the study

We acknowledge that to fully understand the mechanism by which $MORF_{WH1}$ associates with $p300_{TAZ2}$ and DNA, an atomic-resolution structure of the three-component complex is needed.

STAR★METHODS

Detailed methods are provided in the online version of this paper and include the following:

- KEY RESOURCES TABLE
- RESOURCE AVAILABILITY
  - Lead contact
  - Materials availability
  - Data and code availability

SUPPLEMENTAL INFORMATION

Supplemental information can be found online at https://doi.org/10.1016/j.isci.2024.109367.

ACKNOWLEDGMENTS

We thank Hagumu Sato, Ikuko Yokoyama, Kanae Ito, Etsuko Kanai and Ayako Yokoyama for technical assistance, members of the Shonai Regional Industry Promotion Center for their administrative support. This work was supported in part by grants from the NIH: HL151334, GM135671, GM125195, CA252707, and AG067664 to T.G.K., and GM139564 to M.G.P., from the Japan Society for the Promotion of Science (JSPS) KAKENHI grants (19H03694, 22H03109, and 22KK0119) to A.Y. This work was also supported in part by research funds from the Yamagata prefectural government and the city of Tsuruoka. B.-R.Z. and Y.B. are supported by the intramural research program of National Cancer Institute, NIH. The content is solely the responsibility of the authors and does not necessarily represent the official views of the NIH.

AUTHOR CONTRIBUTIONS

D.C.B., A.K., S.B., M.H., and K.L.C. performed experiments and together with L.Z., M.G.P., M.-M.Z., X.S., A.Y., and T.G.K. analyzed the data and prepared figures. T.G.K. wrote the manuscript with input from all authors.

DECLARATION OF INTERESTS

Author TGK is a member of the iScience Editorial Board and Guest Editor for the Special Issue "Epigenetics drug discovery, delivery and targeting."

Received: November 30, 2023
Revised: February 19, 2024
Accepted: February 26, 2024
Published: February 29, 2024

REFERENCES

1. Grunstein, M. (1997). Histone acetylation in chromatin structure and transcription. Nature *389*, 349–352. https://doi.org/10.1038/38664.
2. Verdin, E., and Ott, M. (2015). 50 years of protein acetylation: from gene regulation to epigenetics, metabolism and beyond. Nat. Rev. Mol. Cell Biol. *16*, 258–264. https://doi.org/10.1038/nrm3931.
3. Klein, B.J., Lalonde, M.E., Côté, J., Yang, X.J., and Kutateladze, T.G. (2014). Crosstalk between epigenetic readers regulates the MOZ/MORF HAT complexes. Epigenetics *9*, 186–193. https://doi.org/10.4161/epi.26792.
4. Yan, F., Li, J., Milosevic, J., Petroni, R., Liu, S., Shi, Z., Yuan, S., Reynaga, J.M., Qi, Y., Rico, J., et al. (2022). KAT6A and ENL Form an Epigenetic Transcriptional Control Module to Drive Critical Leukemogenic Gene-Expression Programs. Cancer Discov. *12*, 792–811. https://doi.org/10.1158/2159-8290.CD-20-1459.
5. Zhao, W., Mo, H., Liu, R., Chen, T., Yang, N., and Liu, Z. (2022). Matrix stiffness-induced upregulation of histone acetyltransferase KAT6A promotes hepatocellular carcinoma progression through regulating SOX2 expression. Br. J. Cancer *127*, 202–210. https://doi.org/10.1038/s41416-022-01784-9.
6. Miyamoto, R., Okuda, H., Kanai, A., Takahashi, S., Kawamura, T., Matsui, H., Kitamura, T., Kitabayashi, I., Inaba, T., and Yokoyama, A. (2020). Activation of CpG-Rich Promoters Mediated by MLL Drives MOZ-Rearranged Leukemia. Cell Rep. *32*, 108200. https://doi.org/10.1016/j.celrep.2020.108200.
7. Yang, X.J. (2015). MOZ and MORF acetyltransferases: Molecular interaction, animal development and human disease. Biochim. Biophys. Acta *1853*, 1818–1826. https://doi.org/10.1016/j.bbamcr.2015.04.014.
8. Troisi, S., Maitz, S., Severino, M., Spano, A., Cappuccio, G., Brunetti-Pierri, N., Torella, A., Nigro, V., Tudp, Bilo, L., Bilo, L., and Coppola, A. (2022). Epilepsy in KAT6A syndrome: Description of two individuals and revision of the literature. Eur. J. Med. Genet. *65*, 104380. https://doi.org/10.1016/j.ejmg.2021.104380.
9. Trinh, J., Hüning, I., Yüksel, Z., Baalmann, N., Imhoff, S., Klein, C., Rolfs, A., Gillessen-Kaesbach, G., and Lohmann, K. (2018). A KAT6A variant in a family with autosomal dominantly inherited microcephaly and developmental delay. J. Hum. Genet. *63*, 997–1001. https://doi.org/10.1038/s10038-018-0469-0.
10. Klein, B.J., Jang, S.M., Lachance, C., Mi, W., Lyu, J., Sakuraba, S., Krajewski, K., Wang, W.W., Sidoli, S., Liu, J., et al. (2019). Histone H3K23-specific acetylation by MORF is coupled to H3K14 acylation. Nat. Commun. *10*, 4724. https://doi.org/10.1038/s41467-019-12551-5.
11. Qiu, Y., Liu, L., Zhao, C., Han, C., Li, F., Zhang, J., Wang, Y., Li, G., Mei, Y., Wu, M., et al. (2012). Combinatorial readout of unmodified H3R2 and acetylated H3K14 by the tandem PHD finger of MOZ reveals a regulatory mechanism for HOXA9 transcription. Genes Dev. *26*, 1376–1391. https://doi.org/10.1101/gad.188359.112.

12. Ali, M., Yan, K., Lalonde, M.E., Degerny, C., Rothbart, S.B., Strahl, B.D., Côté, J., Yang, X.J., and Kutateladze, T.G. (2012). Tandem PHD fingers of MORF/MOZ acetyltransferases display selectivity for acetylated histone H3 and are required for the association with chromatin. J. Mol. Biol. *424*, 328–338. https://doi.org/10.1016/j.jmb.2012.10.004.
13. Klein, B.J., Simithy, J., Wang, X., Ahn, J., Andrews, F.H., Zhang, Y., Côté, J., Shi, X., Garcia, B.A., and Kutateladze, T.G. (2017). Recognition of Histone H3K14 Acylation by MORF. Structure *25*, 650–654.e2. https://doi.org/10.1016/j.str.2017.02.003.
14. Holbert, M.A., Sikorski, T., Carten, J., Snowflack, D., Hodawadekar, S., and Marmorstein, R. (2007). The human monocytic leukemia zinc finger histone acetyltransferase domain contains DNA-binding activity implicated in chromatin targeting. J. Biol. Chem. *282*, 36603–36613. https://doi.org/10.1074/jbc.M705812200.
15. Dreveny, I., Deeves, S.E., Fulton, J., Yue, B., Messmer, M., Bhattacharya, A., Collins, H.M., and Heery, D.M. (2014). The double PHD finger domain of MOZ/MYST3 induces alpha-helical structure of the histone H3 tail to facilitate acetylation and methylation sampling and modification. Nucleic Acids Res. *42*, 822–835. https://doi.org/10.1093/nar/gkt931.
16. Xiong, X., Panchenko, T., Yang, S., Zhao, S., Yan, P., Zhang, W., Xie, W., Li, Y., Zhao, Y., Allis, C.D., and Li, H. (2016). Selective recognition of histone crotonylation by double PHD fingers of MOZ and DPF2. Nat. Chem. Biol. *12*, 1111–1118. https://doi.org/10.1038/nchembio.2218.
17. Weber, L.M., Jia, Y., Stielow, B., Gisselbrecht, S.S., Cao, Y., Ren, Y., Rohner, I., King, J., Rothman, E., Fischer, S., et al. (2023). The histone acetyltransferase KAT6A is recruited to unmethylated CpG islands via a DNA binding winged helix domain. Nucleic Acids Res. *51*, 574–594. https://doi.org/10.1093/nar/gkac1188.
18. Becht, D.C., Klein, B.J., Kanai, A., Jang, S.M., Cox, K.L., Zhou, B.R., Phanor, S.K., Zhang, Y., Chen, R.W., Ebmeier, C.C., et al. (2023). MORF and MOZ acetyltransferases target unmethylated CpG islands through the winged helix domain. Nat. Commun. *14*, 697. https://doi.org/10.1038/s41467-023-36368-5.
19. Arany, Z., Sellers, W.R., Livingston, D.M., and Eckner, R. (1994). E1A-associated p300 and CREB-associated CBP belong to a conserved family of coactivators. Cell *77*, 799–800. https://doi.org/10.1016/0092-8674(94)90127-9.
20. Bannister, A.J., and Kouzarides, T. (1996). The CBP co-activator is a histone acetyltransferase. Nature *384*, 641–643. https://doi.org/10.1038/384641a0.
21. Ogryzko, V.V., Schiltz, R.L., Russanova, V., Howard, B.H., and Nakatani, Y. (1996). The transcriptional coactivators p300 and CBP are histone acetyltransferases. Cell *87*, 953–959.
22. Jin, Q., Yu, L.R., Wang, L., Zhang, Z., Kasper, L.H., Lee, J.E., Wang, C., Brindle, P.K., Dent, S.Y.R., and Ge, K. (2011). Distinct roles of GCN5/PCAF-mediated H3K9ac and CBP/p300-mediated H3K18/27ac in nuclear receptor transactivation. EMBO J. *30*, 249–262. https://doi.org/10.1038/emboj.2010.318.
23. Dancy, B.M., and Cole, P.A. (2015). Protein lysine acetylation by p300/CBP. Chem. Rev. *115*, 2419–2452. https://doi.org/10.1021/cr500452k.
24. Goodman, R.H., and Smolik, S. (2000). CBP/p300 in cell growth, transformation, and development. Genes Dev. *14*, 1553–1577.
25. Bedford, D.C., Kasper, L.H., Fukuyama, T., and Brindle, P.K. (2010). Target gene context influences the transcriptional requirement for the KAT3 family of CBP and p300 histone acetyltransferases. Epigenetics *5*, 9–15.
26. Wang, Z., Zang, C., Cui, K., Schones, D.E., Barski, A., Peng, W., and Zhao, K. (2009). Genome-wide mapping of HATs and HDACs reveals distinct functions in active and inactive genes. Cell *138*, 1019–1031. https://doi.org/10.1016/j.cell.2009.06.049.
27. Visel, A., Blow, M.J., Li, Z., Zhang, T., Akiyama, J.A., Holt, A., Plajzer-Frick, I., Shoukry, M., Wright, C., Chen, F., et al. (2009). ChIP-seq accurately predicts tissue-specific activity of enhancers. Nature *457*, 854–858. https://doi.org/10.1038/nature07730.
28. Yao, T.P., Oh, S.P., Fuchs, M., Zhou, N.D., Ch'ng, L.E., Newsome, D., Bronson, R.T., Li, E., Livingston, D.M., and Eckner, R. (1998). Gene dosage-dependent embryonic development and proliferation defects in mice lacking the transcriptional integrator p300. Cell *93*, 361–372. https://doi.org/10.1016/s0092-8674(00)81165-4.
29. Wang, F., Marshall, C.B., and Ikura, M. (2013). Transcriptional/epigenetic regulator CBP/p300 in tumorigenesis: structural and functional versatility in target recognition. Cell. Mol. Life Sci. *70*, 3989–4008. https://doi.org/10.1007/s00018-012-1254-4.
30. Lasko, L.M., Jakob, C.G., Edalji, R.P., Qiu, W., Montgomery, D., Digiammarino, E.L., Hansen, T.M., Risi, R.M., Frey, R., Manaves, V., et al. (2017). Discovery of a selective catalytic p300/CBP inhibitor that targets lineage-specific tumours. Nature *550*, 128–132. https://doi.org/10.1038/nature24028.
31. Iyer, N.G., Ozdag, H., and Caldas, C. (2004). p300/CBP and cancer. Oncogene *23*, 4225–4231. https://doi.org/10.1038/sj.onc.1207118.
32. Delvecchio, M., Gaucher, J., Aguilar-Gurrieri, C., Ortega, E., and Panne, D. (2013). Structure of the p300 catalytic core and implications for chromatin targeting and HAT regulation. Nat. Struct. Mol. Biol. *20*, 1040–1046. https://doi.org/10.1038/nsmb.2642.
33. Park, S., Stanfield, R.L., Martinez-Yamout, M.A., Dyson, H.J., Wilson, I.A., and Wright, P.E. (2017). Role of the CBP catalytic core in intramolecular SUMOylation and control of histone H3 acetylation. Proc. Natl. Acad. Sci. USA *114*, E5335–E5342. https://doi.org/10.1073/pnas.1703105114.
34. Zhang, Y., Xue, Y., Shi, J., Ahn, J., Mi, W., Ali, M., Wang, X., Klein, B.J., Wen, H., Li, W., et al. (2018). The ZZ domain of p300 mediates specificity of the adjacent HAT domain for histone H3. Nat. Struct. Mol. Biol. *25*, 841–849. https://doi.org/10.1038/s41594-018-0114-9.
35. Thompson, P.R., Wang, D., Wang, L., Fulco, M., Pediconi, N., Zhang, D., An, W., Ge, Q., Roeder, R.G., Wong, J., et al. (2004). Regulation of the p300 HAT domain via a novel activation loop. Nat. Struct. Mol. Biol. *11*, 308–315. https://doi.org/10.1038/nsmb740.
36. Ortega, E., Rengachari, S., Ibrahim, Z., Hoghoughi, N., Gaucher, J., Holehouse, A.S., Khochbin, S., and Panne, D. (2018). Transcription factor dimerization activates the p300 acetyltransferase. Nature *562*, 538–544. https://doi.org/10.1038/s41586-018-0621-1.
37. Xu, L., Xuan, H., He, W., Zhang, L., Huang, M., Li, K., Wen, H., Xu, H., and Shi, X. (2023). TAZ2 truncation confers overactivation of p300 and cellular vulnerability to HDAC inhibition. Nat. Commun. *14*, 5362. https://doi.org/10.1038/s41467-023-41245-2.
38. Ibrahim, Z., Wang, T., Destaing, O., Salvi, N., Hoghoughi, N., Chabert, C., Rusu, A., Gao, J., Feletto, L., Reynoird, N., et al. (2022). Structural insights into p300 regulation and acetylation-dependent genome organisation. Nat. Commun. *13*, 7759. https://doi.org/10.1038/s41467-022-35375-2.
39. Ferreon, J.C., Lee, C.W., Arai, M., Martinez-Yamout, M.A., Dyson, H.J., and Wright, P.E. (2009). Cooperative regulation of p53 by modulation of ternary complex formation with CBP/p300 and HDM2. Proc. Natl. Acad. Sci. USA *106*, 6591–6596. https://doi.org/10.1073/pnas.0811023106.
40. Brown, A.D., Cranstone, C., Dupré, D.J., and Langelaan, D.N. (2023). beta-Catenin interacts with the TAZ1 and TAZ2 domains of CBP/p300 to activate gene transcription. Int. J. Biol. Macromol. *238*, 124155. https://doi.org/10.1016/j.ijbiomac.2023.124155.
41. Lochhead, M.R., Brown, A.D., Kirlin, A.C., Chitayat, S., Munro, K., Findlay, J.E., Baillie, G.S., LeBrun, D.P., Langelaan, D.N., and Smith, S.P. (2020). Structural insights into TAZ2 domain-mediated CBP/p300 recruitment by transactivation domain 1 of the lymphopoietic transcription factor E2A. J. Biol. Chem. *295*, 4303–4315. https://doi.org/10.1074/jbc.RA119.011078.
42. Harami, G.M., Gyimesi, M., and Kovács, M. (2013). From keys to bulldozers: expanding roles for winged helix domains in nucleic-acid-binding proteins. Trends Biochem. Sci. *38*, 364–371. https://doi.org/10.1016/j.tibs.2013.04.006.
43. Delaglio, F., Grzesiek, S., Vuister, G.W., Zhu, G., Pfeifer, J., and Bax, A. (1995). NMRPipe: a multidimensional spectral processing system based on UNIX pipes. J. Biomol. NMR *6*, 277–293.
44. Skinner, S.P., Fogh, R.H., Boucher, W., Ragan, T.J., Mureddu, L.G., and Vuister, G.W. (2016). CcpNmr AnalysisAssign: a flexible platform for integrated NMR analysis. J. Biomol. NMR *66*, 111–124. https://doi.org/10.1007/s10858-016-0060-y.
45. Shen, L., Shao, N., Liu, X., and Nestler, E. (2014). ngs.plot: Quick mining and visualization of next-generation sequencing data by integrating genomic databases. BMC Genom. *15*, 284. https://doi.org/10.1186/1471-2164-15-284.
46. Musselman, C.A., Gibson, M.D., Hartwick, E.W., North, J.A., Gatchalian, J., Poirier, M.G., and Kutateladze, T.G. (2013). Binding of PHF1 Tudor to H3K36me3 enhances nucleosome accessibility. Nat. Commun. *4*, 2969. https://doi.org/10.1038/ncomms3969.
47. Okuda, H., Kawaguchi, M., Kanai, A., Matsui, H., Kawamura, T., Inaba, T., Kitabayashi, I., and Yokoyama, A. (2014). MLL fusion proteins link transcriptional coactivators to previously active CpG-rich promoters. Nucleic Acids Res. *42*, 4241–4256. https://doi.org/10.1093/nar/gkt1394.
48. Thorvaldsdóttir, H., Robinson, J.T., and Mesirov, J.P. (2013). Integrative Genomics

Viewer (IGV): high-performance genomics data visualization and exploration. Brief. Bioinform. *14*, 178–192. https://doi.org/10.1093/bib/bbs017.

49. Klein, B.J., Piao, L., Xi, Y., Rincon-Arano, H., Rothbart, S.B., Peng, D., Wen, H., Larson, C., Zhang, X., Zheng, X., et al. (2014). The Histone-H3K4-Specific Demethylase KDM5B Binds to Its Substrate and Product through Distinct PHD Fingers. Cell Rep. *6*, 325–335. https://doi.org/10.1016/j.celrep.2013.12.021.

50. Tencer, A.H., Cox, K.L., Di, L., Bridgers, J.B., Lyu, J., Wang, X., Sims, J.K., Weaver, T.M., Allen, H.F., Zhang, Y., et al. (2017). Covalent Modifications of Histone H3K9 Promote Binding of CHD3. Cell Rep. *21*, 455–466. https://doi.org/10.1016/j.celrep.2017.09.054.

STAR★METHODS

KEY RESOURCES TABLE

REAGENT or RESOURCE	SOURCE	IDENTIFIER
Antibodies		
anti-MOZ antibody	Active motif	Cat. # 39868; Discontinued
anti-Histone H3K18ac antibody	Abcam	Cat. # ab1191; RRID: AB_298692
anti-RNA Polymerase II (RNAP2 non-P) antibody	Abcam	Cat. # ab817; RRID: AB_306327
anti-FLAG antibody	Sigma-Aldrich	Cat. # F3165; RRID: AB_259529
Bacterial and virus strains		
Escherichia coli BL21 (DE3) Rosetta2 pLysS	Kutateladze lab	N/A
Chemicals, peptides, and recombinant proteins		
$^{15}NH_4Cl$	Sigma-Aldrich	Cat. # 299251
$ZnCl_2$	Sigma-Aldrich	Cat. # 229997
Multivitamin Tablet	Centrum Walmart	Cat. # 573963323
DNase I	Sigma-Aldrich	Cat. # 10104159001
Deuterium oxide (D_2O)	Sigma-Aldrich	Cat. # D4501
QIAprep Spin Miniprep Kit	Qiagen	Cat. # 27104
QuikChange Lightning Site-Directed Mutagenesis Kit	Agilent Technologies	Cat. # 210518
PureLink HiPure Expi Plasmid Gigaprep Kit	Invitrogen	Cat. # K210009XP
Tobacco Etch Virus (TEV) protease	Home expressed	N/A
SYBR Gold	ThermoFisher Sci.	Cat. # S11494
$MORF_{TAD}$ (aa 3-23)	SynPeptide	N/A
Deposited data		
Sample IDs and GEA accession numbers of the NGS data (ID; accession number), also see Table S1	GEA	https://www.ddbj.nig.ac.jp/dra/index.html https://ddbj.nig.ac.jp/public/ddbj_database/gea/experiment/E-GEAD-000/ SAMD00180208; E-GEAD-324 SAMD00180209; E-GEAD-324 SAMD00180127; E-GEAD-322 SAMD00247201; E-GEAD-402 SAMD00393839; E-GEAD-446 SAMD00180131; E-GEAD-322 SAMD00495574; E-GEAD-498 SAMD00495575; E-GEAD-498 SAMD00567465; E-GEAD-584
Accession number for NMR assignments of $p300_{TAZ2}$	BMRB	https://bmrb.io/ ID 52222
Experimental models: Cell lines		
Human: HEK293T	ATCC	Cat. # CRL-3216; RRID: CVCL_0063

(*Continued on next page*)

Continued

REAGENT or RESOURCE	SOURCE	IDENTIFIER
Oligonucleotides		
Primers: TAZ2 A1723W F: 5′-GAACCTGTACTTCCAATCTAATGCT TGGACCCAGAGCCCAG-3′ R: 5′-CTGGGCTCTGGGTCCAAGCATTAG ATTGGAAGTACAGGTTC-3′	Integrated DNA Technologies, Inc.	N/A
Primers: TAZ2 1813X F: 5′-CCTAAACATCAAGCAGAAGTAGCGG CAGCAACAGTTCCAGC-3′ R: 5′-GCTGGAACTGTTGCTGCCGCTACTT CTGCTTGATGTTTAGG-3′	Integrated DNA Technologies, Inc.	N/A
Primers: TAZ2 6xHis-Insert F: 5′-GCAGAAGCATCATCACCATCACCAC TAGCGGCAGCAACAGTTCC-3′ R: 5′-CGCTAGTGGTGATGGTGATGATGCT TCTGCTTGATGTTTAGGCAGAAC-3′	Integrated DNA Technologies, Inc.	N/A
Duplex DNA: DNA_{16} (CpG-rich) F: 5′-TAACCTGCGCACCATA-3′ R: 5′-TATGGTGCGCAGGTTA-3′	Integrated DNA Technologies, Inc.	N/A
Duplex DNA: DNA_{15} (A/T-rich) F: 5′-GCAAAAAAAAAAACG-3′ R: 5′-CGTTTTTTTTTTTGC-3′	Integrated DNA Technologies, Inc.	N/A
Duplex DNA: DNA_{147} (601 Widom Sequence)	Home expressed	N/A
Recombinant DNA		
pDEST17 MORF WH1 (aa 5-84)	Kutateladze lab	N/A
pGEX4TEV MOZ WH1 (aa 1-86)	Kutateladze lab	N/A
pET22b MOZ WH1 (aa 2-86)-6xHis	Kutateladze lab	N/A
pGEX-6P-1 p300 TAZ2 (aa 1722-1836)	Kutateladze lab	N/A
pGEX-6P-1 p300 TAZ2 (aa 1722-1812)	Kutateladze lab	N/A
Software and algorithms		
NMRPipe	Delaglio et al.[43]	https://www.ibbr.umd.edu/nmrpipe/
CcpNmr AnalysisAssign (V3)	Skinner et al.[44]	https://ccpn.ac.uk/software/
GraphPad Prism	GraphPad Software, Inc.	https://www.graphpad.com/scientific-software/prism/
MO.Affinity Analysis	NanoTemper Technologies	https://nanotempertech.com/monolith-mo-control-software/
MO.Control software	NanoTemper Technologies	https://nanotempertech.com/monolith-mo-control-software/
Integrative Genomics Viewer		https://software.broadinstitute.org/software/igv/
ngsplot	Shen et al.[45]	https://github.com/shenlab-sinai/ngsplot
Other		
HiLoad Superdex 75 pg column	Cytiva	Cat. # 28989333
HiTrap SP HP	Cytiva	Cat. # 17115201
Amicon Ultra 15 mL 3K NMWL centrifugal filter unit	Millipore	Cat. # UFC900308
Varian INOVA 600 MHz NMR spectrometer	Agilent Technologies	N/A
Glutathione Sepharose 4B beads	Thermo Fisher Sci.	Cat. # 16101
Ni-NTA resin	Thermo Fisher Sci.	Cat. # 88223

RESOURCE AVAILABILITY

Lead contact

Further information and requests for resources and reagents should be directed to and will be fulfilled upon reasonable request by the lead contact, Tatiana G. Kutateladze (tatiana.kutateladze@cuanschutz.edu).

Materials availability

All expression plasmids used in this study will be made available on request. This study did not generate new unique reagents.

Data and code availability

- ChIP-seq data and CIRA-seq data have been deposited at the DDBJ (DNA Data Bank of Japan) and are publicly available as of the date of publication. Accession numbers are listed in Table S1 and key resources table. Backbone chemical shift assignments for the apo-state of $p300_{TAZ2}$ have been deposited to the BMRB databank, with accession number listed in key resources table.
- This paper does not report original code.
- Any additional information required to reanalyze the data reported in this paper is available from the lead contact upon request.

EXPERIMENTAL MODEL AND STUDY PARTICIPANT DETAILS

MORF, MOZ and p300 constructs were expressed in Rosetta2 (DE3) pLysS cells in Luria Broth or isotopically enriched media. Protein production was induced with 0.2-0.5 mM IPTG overnight at 16°C.

METHOD DETAILS

Protein purification

Human $MORF_{WH1}$ (aa 5-84, with C-terminal 6xHis tag), MOZ_{WH1} (aa 1-86, with C-terminal 6xHis tag) and MOZ_{WH1} (aa 2-86) were purified as in.[18] $p300_{TAZ2}$ (aa 1722-1812) was cloned into a pGEX-4P-1 vector with an additional TEV cleavage site. Mutant constructs, $p300_{TAZ2}$ (A1723W) and $p300_{TAZ2}$ with a C-terminal His tag, were generated using the QuikChange Lightning kit (Stratagene). All constructs were confirmed by DNA sequencing. Unlabeled and ^{15}N-labeled proteins were expressed in *E. coli* Rosetta-2 (DE3) pLysS cells grown in TB or minimal media supplemented with $^{15}NH_4Cl$ (Sigma-Aldrich) and additionally with 50-150 μM $ZnCl_2$ for expression of $p300_{TAZ2}$ proteins. After induction with IPTG (final concentration 0.2-0.5 mM, Gold Biotechnology) for 16 hrs at 16°C, cells were harvested via centrifugation and lysed in buffer (Tris pH 7.0-7.5, 500 mM NaCl, 5 mM dithiothreitol (DTT), phenylmethanesulfonylfluoride (PMSF), and DNase) by sonication. The unlabeled and ^{15}N-labeled GST fusion proteins were purified on glutathione agarose beads (Pierce) and eluted with buffer supplemented with 10-50 mM reduced L-glutathione (Fisher). The GST-tag was cleaved with tobacco etch virus (TEV) protease overnight at 22°C. His-tagged fusion proteins were purified using nickel–NTA resin (ThermoFisher) and eluted from the resin with a buffered gradient of imidazole. Proteins were further purified by size exclusion chromatography (SEC) or cation exchange chromatography ($p300_{TAZ2}$ only) and concentrated in Millipore concentrators.

DNA purification

Double stranded DNA containing the 601 Widom sequence cloned into the pJ201 plasmid (147 bp) was transformed into DH5α cells. The plasmids were purified either as previously described[46] or by the PureLink HiPure Expi Plasmid Gigaprep Kit (Invitrogen K210009XP). Separation of the individual sequences was completed by digestion of the plasmid with EcoRV followed by PEG and ethanol precipitation. Short DNAs were ordered as pre-annealed double stranded DNA (Integrated DNA Technologies).

EMSA

Increasing amounts of $MORF_{WH1}$ were incubated with DNA_{147} (10 nM, 601 Widom sequence) or DNA_{16} (100 nM, CpG-rich) in buffer (20 mM Tris HCl pH 7.5, 150 mM NaCl, 5 mM DTT) in a 10 μL reaction volume, with or without $p300_{TAZ2}$ (2 μM, i.e. ~10 x K_d), or increasing amounts of $p300_{TAZ2}$ were incubated with DNA_{147} in the same buffer and reaction volume. 2 μl of loading dye was added to each sample and loaded onto an 8% native polyacrylamide gel. Electrophoresis was performed in 0.2 × TBE buffer (1 × TBE = 90 mM Tris, 94 mM boric acid, and 2 mM EDTA) at 100 V on ice. Gels were stained with SYBR Gold (Thermo Fisher Scientific) and visualized by Blue LED (UltraThin LED Illuminator, Gel Company Inc).

Cell lines

HEK293T cells were purchased from ATCC. Cells were cultured in Dulbecco's modified Eagles medium, supplemented with 10% fetal bovine serum and penicillin-streptomycin. Cells were cultured in an incubator at 37°C and 5% CO_2 and routinely tested for mycoplasma using a MycoAlert Mycoplasma Detection Kit (Lonza).

ChIP-seq

Chromatin fractions from HEK293T cells were prepared using the fanChIP method as previously described.[47] Cells were suspended in CSK buffer and centrifuged to remove the soluble fraction in the same manner as the nucfrIP analysis. The pellet was resuspended in MNase buffer and treated with MNase at 37°C for 3-6 min to obtain oligonucleosomes. The MNase reaction was stopped by adding EDTA (pH 8.0) to a final concentration of 20 mM. Lysis buffer (250 mM NaCl, 20 mM sodium phosphate [pH 7.0], 30 mM sodium pyrophosphate, 5 mM EDTA, 10 mM NaF, 0.1% NP-40, 10% glycerol, 1 mM DTT, and EDTA-free protease inhibitor cocktail) was added to increase solubility. The chromatin fraction was cleared by centrifugation and subjected to immunoprecipitation with specific antibodies and magnetic microbeads (Protein-G magnet beads [Invitrogen]. Immunoprecipitates were washed five times with washing buffer (1:1 mixture of lysis buffer and MNase buffer with 20 mM EDTA) and then eluted in elution buffer. The eluted material was extracted by phenol/chloroform/isoamyl alcohol. DNA was precipitated with glycogen (Nacalai Tesque), dissolved in TE, and analyzed by qPCR and deep sequencing. CpG island recovery assays for unmethylated CpGs (CIRA) were performed using the Unmethyl Collector kit (Active Motif). For deep sequencing, Purified DNA was further fragmented (~150 bp long) using the Covaris M220 DNA shearing system (M&M Instruments Inc.). Deep sequencing was performed using a TruSeq ChIP Sample Prep Kit (Illumina) and HiSeq2500 (Illumina) at the core facility of Hiroshima University. Approximately 19 to 47 million single end reads were obtained, of which 15 to 41 million reads were mapped to the genome and are subjected to further analysis. Data were visualized using the Integrative Genome Viewer (Broad Institute).[48] Heatmaps of ChIP signals on each TSS were generated by ngsplot.[45]

ChIP-seq data and CIRA-seq data have been deposited at the DDBJ (DNA Data Bank of Japan) Sequence Read Archive as fastq files [https://ddbj.nig.ac.jp/public/ddbj_database/dra/fastq/] and as WIG files [https://ddbj.nig.ac.jp/public/ddbj_database/gea/experiment/E-GEAD-000/] under the accession numbers listed in Table S1.

NMR experiments

Nuclear magnetic resonance (NMR) experiments were performed at 298 K on Varian 600 and 900 MHz spectrometers. The ^{1}H,^{15}N HSQC spectra of 50-100 μM uniformly ^{15}N-labeled proteins were collected in the presence of an increasing amount of unlabeled protein, peptide or DNA (IDT). NMR data were processed and analyzed with NMRPipe and NMRDraw as previously described.[49] Normalized chemical shift changes were calculated using the equation,

$$\Delta\delta = \sqrt{(\Delta\delta H)^2+(0.14 * \Delta\delta N)^2}$$

where Δδ is the change in chemical shift in parts per million (ppm).

Backbone chemical shift assignments for $MORF_{WH1}$ were obtained by collecting and processing a set of triple resonance experiments (HNCACB, CBCA(CO)NH, HNCA, HNCO, and HN(CA)CO) with non-uniform sampling (the assignment is available from the lead contact on request). Backbone chemical shift assignments for the apo-state of $p300_{TAZ2}$ were obtained from ^{15}N-edited NOESY-HSQC and deposited to the BMRB databank (ID 52222). NMR spectra were processed and analyzed with NMRPipe, NMRDraw, and the CcpNmr Suite.[43,44]

MST

Microscale thermophoresis (MST) experiments were performed on a Monolith NT.115 instrument (NanoTemper). Experiments were performed using purified $p300_{TAZ2}$-His protein in a buffer containing 50 mM Tris pH 7.5, 150 mM NaCl. $p300_{TAZ2}$-His was labeled using a His-Tag Labeling Kit RED-tris-NTA (2nd Generation, NanoTemper) and kept constant at 20 nM. Dissociation constant was determined using a direct binding assay in which unlabeled $MORF_{TAD}$ (aa 3-23) (SynPeptide) was varied in concentration by serial dilution of discrete samples. The measurements were performed at 40% LED and medium MST power with 3 s pre-laser time, 20 s laser on-time and 1 s off-time. The K_d values were calculated using MO Affinity Analysis software (NanoTemper) (n=3). Plots were generated in GraphPad PRISM.

Fluorescence polarization

Nucleosomes (NCPs) were reconstituted as described in.[18] DNAs used in fluorescence polarization were 147 bp 601 Widom DNA fluorescein-labeled on the 5′ end (for NCP_{147}) and 207 bp DNA (147 bp 601 DNA flanked with 30 bp linker DNA on either side and internally labeled with fluorescein 27 bp in from the 5′ end) (for NCP_{207}). Fluorescence polarization measurements were carried out by mixing increasing amounts of MOZ_{WH1}-His with 5 nM NCP_{207} or NCP_{147} in 75 mM NaCl, 25 mM Tris-HCl pH 7.5, 0.00625% Tween20, and 5 mM dithiothreitol in a 30 μL reaction volume. The samples were loaded into a Corning round bottom polystyrene plate and allowed to incubate at 4°C for 30 min. The polarization measurements were acquired with a Tecan infinite M1000Pro plate reader by exciting at 470 nm and measuring polarized emission at 519 nm with 5 nm excitation and emission bandwidths. The fluorescence polarization was calculated from the emission polarized parallel and perpendicular to the polarized excitation light as described previously.[50] The data were then fit to a non-cooperative binding isotherm to determine $S_{1/2}$. The $S_{1/2}$ values were averaged over three separate experiments with error calculated as the standard deviation between the runs.

QUANTIFICATION AND STATISTICAL ANALYSIS

MST assay shown in Figure 4C was performed in three independent replicates. The K_d value was calculated using MO Affinity Analysis software (NanoTemper). Plots were generated in GraphPad PRISM. Data and the K_d value represent the average ± SEM of three independent experiments. Fluorescence polarization assays shown in Figure S3 were performed in three independent replicates. The $S_{1/2}$ values were averaged over three separate experiments with error calculated as the standard deviation between the runs.